Carbon 147 (2019) 58–69

Contents lists available at ScienceDirect

Carbon

journal homepage: www.elsevier.com/locate/carbon

Anisotropic thermal conductivities and structure in lignin-based microscale carbon fibers

Ridong Wang [a, 1], Hamidreza Zobeiri [a, 1], Huan Lin [b], Wangda Qu [a], Xianglan Bai [a], Cheng Deng [c, **], Xinwei Wang [a, *]

[a] Department of Mechanical Engineering, Iowa State University, Ames, IA, 50011, United States
[b] School of Environmental and Municipal Engineering, Qingdao University of Technology, Qingdao, Shandong, 266033, PR China
[c] College of Mechatronics Engineering, Guangdong Polytechnic Normal University, Guangzhou, 510635, PR China

ARTICLE INFO

Article history:
Received 13 December 2018
Received in revised form
17 February 2019
Accepted 19 February 2019
Available online 25 February 2019

ABSTRACT

It is very important to know whether the thermal conductivity of carbon fibers in the directions of fiber axis (axial thermal conductivity, κ_a) and fiber radius (radial thermal conductivity, κ_r) are anisotropic. Relevant measurement is strongly hindered by microsize of carbon fibers in the radial direction. In this work, a novel method by combining frequency domain energy transport state-resolved Raman and transient electrothermal techniques is developed to overcome this drawback to achieve thermal conductivity anisotropy study of lignin-based microscale carbon fibers. Four fibers are characterized and the difference of κ_a among them is very small, and κ_a is around 1.8 W m^{-1} K^{-1} while the difference of κ_r is very large. The κ_r varies from 0.11 to 8.0 W m^{-1} K^{-1}, revealing strong structure anisotropy and radial structure variation. The thermal conductivity variation against temperature also shows very different behavior. κ_a features a reduction of more than one order of magnitude from room temperature to 10.4 K while κ_r shows very little change from room temperature to 77 K. For the same carbon fiber, there is also a large difference of κ_r at different axial positions. Detailed Raman study of the axial and radial structures uncovers very strong structure anisotropy and explains the observed anisotropic thermal conductivities.

1. Introduction

Carbon fiber (CF) is one kind of materials that permits the integration of high-performance and rich functionalities [1–4]. The three most important precursors for CF production are polyacrylonitrile (PAN) [5], mesophase pitch (MPP) [6,7] and lignin [8–10]. Currently, CF has been widely used in aerospace structures [11], nuclear reactors [12], turbine blades [13], etc. In these applications, measuring the thermal conductivity of single CF has attracted much attention due to the fundamental role in evaluating the heat transfer characteristics of CFs. In addition, a single CF is also very promising to be used in thermal management and design in microelectric and micromechanic fields [14–16]. Therefore, it is also very important to understand the thermal conductivity of a single CF. However, it is still very challenging to measure the radial direction thermal conductivity of a CF since it has a diameter of several tens of microns or less.

Some previous studies have reported the axial thermal conductivity direction of different carbon fibers by using different methods. Zhang et al. [17] used the steady-state shot-hot-wire method to measure the thermal conductivity of a single CF. The thermal conductivity of the single CF was determined based on the relations among the average temperature rise of the hot wire, the heat generation rate, the temperature at the attached end of the fiber, and the heat flux from the hot wire to the fiber. Gallego et al. [18] measured the thermal conductivity of ribbon-shaped fibers by two methods: a thermal potentiometer as a steady-state apparatus to measure CF's thermal response to a controlled thermal gradient, and an Angstrom's method to measure CF's thermal response to an oscillating heat input. Wang et al. [19] used a T type method to measure the thermal conductivity of individual pitch-derived CFs in the temperature range of 100–400 K. In this method, a hot wire served as both a heating source and a thermometer. The thermal conductivity of CF was determined by comparing the average

** Corresponding author.
* Corresponding author.
E-mail addresses: dengcheng1986@gmail.com (C. Deng), xwang3@iastate.edu (X. Wang).
[1] These authors contributed equally to the work.

https://doi.org/10.1016/j.carbon.2019.02.064
0008-6223/

temperature rise of the hot wire with and without the CF. Emmerich [20] presented a model of continuous defective graphene nanoribbons to predict the thermal conductivity of mesophase pitch-based carbon fibers in a single physical framework. Pradere et al. [21] measured the specific heat and the longitudinal thermal diffusivity (α) of three carbon fibers (rayon-based, polyacrylonitrile-based and pitch-based). Then, the thermal conductivity (κ) of these carbon fibers was calculated by the relation $\kappa = \alpha\rho c_p$, where ρc_p was the volumetric heat capacity of the sample. Qiu et al. [22] used a modified 3ω method to measure the thermal conductivity of an individual polyacrylonitrile-based CFs processed under different treatment temperatures. Yuan et al. [23] calculated the thermal conductivities of the various round-shaped CFs according to the relationship between electrical resistivity and thermal conductivity. Liu et al. [24] measured the thermal conductivity of the CFs from room temperature (RT) down to 10 K by the cryogenic TET technique.

Though different methods have been used to measure the thermal conductivity of CFs, only the axial thermal conductivity is obtained. The radial thermal conductivity has never been measured and understood while such data is critical to understand the structure anisotropy. To date, it is unknown whether the radial thermal conductivity and the axial thermal conductivity of CFs are anisotropic or not. In this work, we develop a novel method by combining the frequency domain energy transport state-resolved Raman (FET-Raman) technique with the transient electrothermal (TET) technique to measure the axial and radial thermal conductivities of lignin-based CFs. The temperature effect on the thermal conductivities in the two directions is explored. The temperature ranges from 77 K to RT for radial thermal conductivity measurement, and from 10.4 K to RT for axial thermal conductivity measurement.

2. Sample preparation and characterization

The carbon fibers used in this work are synthesized from pyrolytic lignin (PL). PL is obtained by pyrolyzing red oak at 500 °C, and collected as stage fraction 1(SF1) of the vapor condensates [25]. SF1 is further washed with deionized water three times to remove sugars. The water washed PL is thermally treated at 105–130 °C with addition of sulfuric acid as catalyst [26]. The obtained PL precursor is subjected to melt-spinning at 140–150 °C with a winding speed of 50 m/min to get the as-spun fiber. The as-spun fiber is mounted on a metal rack and oxidatively stabilized in a convection oven at 0.3 °C/min from RT to 250 °C, and then is held at 250 °C for another 1 h. Then the stabilized fiber is carbonized in a tubular furnace with argon as carrier gas. The heating program used for carbonization is 3 °C/min from RT to 1000 °C, and then held at 1000 °C for another 1 h. Typical scanning electron microscope (SEM) images of the produced carbon fiber are shown in Fig. 1. As shown in Fig. 1(a), the diameters of the four CFs are all around 50 μm. Fig. 1(b) and (c) are the SEM images to zoom in the surface and cross-section of a single CF. As shown in these two figures, the surface of the CF is smooth, and the cross-section has a very good circular shape.

X-ray diffraction (XRD) and X-ray photoelectron spectroscopy (XPS) have been used to study the microstructure and elemental composition of the CFs in our previous work [24]. Two broad peaks were observed at 23.53° and 43.18° in XRD characterization, corresponding to (002) peak and (100) peak in the XRD results. Then, the lattice spacing of (002) peak was determined to be 0.378 nm. For PAN-based CFs, the value was 0.3395–0.353 nm. And for highly graphitized carbon, this value should be less than 0.344 nm [27–29]. As a result, non-graphitizable carbon with turbostratic structure and a certain small amount of cross-links may exist in the lignin-based CFs.

The XRD result also indicated low crystallinity of the CFs. Based on our previous XRD results, the crystallite size was determined at 0.9 nm in the cross-plane direction (002) and 1.2 nm in the in-plane direction (100). The Scherrer constants used for determining these two values were all equal to 0.9. The ratio of the crystallite size in the in-plane direction (L_a) and the crystallite size in the cross-plane direction (L_c), L_a/L_c, was less than 10. This indicated that the CF formed by red oak was graphitizing [30]. However, as the red oak was pyrolyzed at 500 °C, a finely porous structure was likely exhibited. That is, non-graphitizable carbon may exist in the CF [31]. The XPS was used to do the chemical analysis. The elemental composition was determined as: C (93.4%), H (0.74%), and O (4.55%). The functional groups existing in the sample included C–H, C–C, C=C (these three totally 84.83%), C–O (7.87%), and O–C=O (7.29%). And most of the C–O and O–C=O functional groups were situated in the cross-links or defective regions between carbon layers. Due to these functional groups, the lattice spacing between carbon layers was larger than that of PAN-based CFs. Because of the low crystallinity, the axial thermal conductivity of the lignin-based CFs was very low [22,32].

3. Physical principles for anisotropic thermal conductivity characterization

3.1. Characterization of the thermal conductivity in the axial direction

The TET technique is used to determine the thermal conductivity (κ_a) in the axial direction of CF. In our TET measurement, as shown in Fig. 2(a), a single CF is suspended between two aluminum electrodes. Silver paste is used to secure the contact between the sample and the two electrodes. A small step DC current is applied to

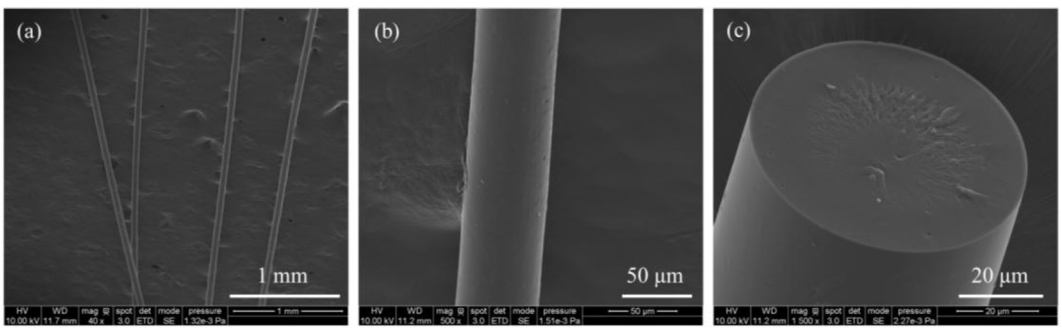

Fig. 1. **(a)** SEM image of several CFs. **(b)** SEM image of the surface for a single CF. **(c)** Cross-sectional view of the CF.

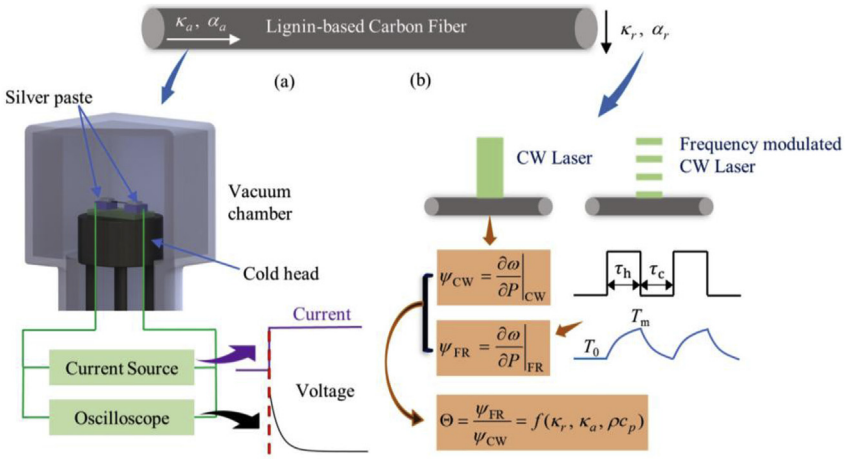

Fig. 2. **(a)** Illustration of the TET technique. A small current is applied over the CF, and the voltage variation is used to probe the temperature change. The axial thermal conductivity of CF can be determined. **(b)** Illustration of the FET-Raman technique. A function generator is used to generate a square wave to modulate the CW laser. Two different energy transport states in the frequency domain with the same objective lens (20 ×) are constructed. The radial thermal conductivity of CF can be obtained. (A colour version of this figure can be viewed online.)

induce Joule heating. The electrical resistance (R) of CF, which is temperature dependent, will decrease during this heating process. As a result, the voltage over the sample will also decrease. And this voltage variation can be used to probe the temperature variation of the sample. Due to the large aspect ratio of CF ($L/D > 32$, L: sample length, D: sample diameter), the governing heat transfer equation of the sample can be considered as a 1-D heat transfer, that is:

$$\frac{\partial(\rho c_p T)}{\partial t} = \kappa_a \frac{\partial^2 T}{\partial x^2} + \dot{q} - \frac{4\varepsilon\sigma\left(T^4 - T_0^4\right)}{D}, \tag{1}$$

where $\dot{q}$ is electrical heating power per unit volume. The term $4\varepsilon\sigma(T^4 - T_0^4)/D$ represents the radiation heat loss, where ε is the surface emissivity and σ is Stefan-Boltzmann constant. The initial condition of this problem is $T(x, t = 0) = T_0$, where T_0 is the initial temperature of the sample. Since the aluminum electrodes are much larger than the sample dimension, they can be considered as thermal reservoirs that their temperature remains unchanged during the electrical heating. As a result, the boundary conditions are $T(x = 0, t) = T(x = L, t) = T_0$. The temperature distribution along the wire can be expressed as $T(x,t) = \int_0^t \int_0^x T(x', \tau) dx' d\tau$ [33], which indicates that the temperature depends on both the position along the fiber and the time. Here $T(x', \tau)$ is the Green's function for the temperature response to a pulse heating at x' and τ. Then, a normalized temperature rise which is defined as $T^*(t) = [T(t) - T_0] / [T(t \to \infty) - T_0]$, where $T(t \to \infty)$ is the temperature at steady state, can be written as below [34]:

$$T^*(t) = \frac{96}{\pi} \sum_{m=1}^{\infty} \frac{1 - \exp\left(-(2m-1)^2 \pi^2 \alpha_{eff} t / L^2\right)}{(2m-1)^4} \tag{2}$$

Here α_{eff} is the effective thermal diffusivity including the radiation effect. We can obtain α_{eff} based on the relation between temperature variation and voltage variation. More details could be found in our previous work [33,35,36]. The real axial thermal diffusivity (α_a) can be obtained by subtracting the contribution of radiation as $\alpha_a = \alpha_{eff} - 16\varepsilon\sigma T^3 L^2 / \pi^2 D \rho c_p$ [24].

Here, we use $\varepsilon = 0.85$ [37]. The effective thermal conductivity (κ_{eff}) can be obtained by comparing the solution at steady state ($t = \infty$) to the solution at initial state ($t = 0$), as $\kappa_{eff} = I^2 RL / 12A\Delta T$ [38], where A is the cross-sectional area of the fiber, and $\Delta T = (R(t \to \infty) - R(t = 0)) / (\partial R / \partial T)$. $\partial R / \partial T$ is obtained from R-T correlation. Additionally, using the obtained α_{eff} and κ_{eff}, we can calculate ρc_p as $\kappa_{eff} / \alpha_{eff}$.

3.2. Characterization of the thermal conductivity in the radial direction

The FET-Raman technique is used to measure the thermal conductivity (κ_r) in the radial direction of CF. In the FET-Raman technique, we probe the thermal response of CF by irradiating the CF using a continuous-wave (CW) laser with 532 nm wavelength. And two energy transport states are constructed with the same laser. Fig. 2(b) shows the physical principle of this technique. The first energy transport state is the steady-state heating. CF will absorb the laser energy and transport it along the axial and radial directions. As κ_a is obtained by using the TET technique, the energy transport in this direction is known. By collecting the excited Raman signals during laser heating, we can obtain the temperature profile of CF. Note here we do not need to measure the real temperature rise of the sample. By using different laser power (P), a parameter called Raman shift power coefficient (RSC) could be obtained: $\psi_{CW} = \partial\omega / \partial P = \alpha(\partial\omega / \partial T) f_1(\kappa_r, \kappa_a)$. ψ_{CW} is determined by laser absorption coefficient (α), temperature coefficient of Raman shift ($\partial\omega / \partial T$), the thermal conductivity in the radial direction (κ_r), and the thermal conductivity in the axial direction (κ_a).

To construct the second energy transport state, a square-wave with a specific frequency is generated to modulate the CW laser amplitude. After a sufficient number of heating cycles, the sample temperature will vary periodically. Compared to the total laser irradiation cycles in the experiment, this time, which is called warm-up time, is short and negligible [39]. In each period of this modulated laser, there is a laser-on time (τ_h) and a laser-off time (τ_c). If the frequency is very low, the temperature of the sample will reach the steady-state during τ_h and return to initial temperature during τ_c. The average temperature rise during τ_h is equal to that under the first energy transport state. This temperature rise is named θ_s. If the frequency is very high, the temperature variation during τ_h and τ_c will be very small, and this variation is almost negligible. As a result, the temperature of the sample can be regarded as a constant after the warm-up process. This state is named quasi-steady state and the temperature rise is named θ_{qs}. With the decrease of frequency, the energy transport state changes from quasi-steady state to steady state, and the corresponding

temperature rise increases from θ_{qs} to θ_s. In our previous study, we found empirically that $\theta_{qs} = \theta_s/2$ within experimental uncertainties [39–41]. To have a good sensitivity, an appropriate frequency is needed to construct the second energy transport state. In this work, the modulation frequency is selected for different CFs and different temperatures. And the selected frequencies are all around the middle of quasi-steady state to steady state range based on our preliminary study. Similarly, by using different laser power, the RSC value could also be obtained: $\psi_{FR} = \partial\omega/\partial P = \alpha(\partial\omega/\partial T)f_2(\kappa_r, \kappa_a, \rho c_p)$. ψ_{FR} is determined by laser absorption coefficient, temperature coefficient of Raman shift, volumetric heat capacity, and the thermal conductivities in the two directions. And the thermal diffusion length in the two directions are different from the steady state. That is, the contribution of heat conduction, which is highly related to the thermal conductivity of CF, to the two RSCs are different for the two cases.

Based on these two RSCs, a dimensionless normalized RSC is defined as $\Theta = \psi_{FR}/\psi_{CW} = f_3(\kappa_r, \kappa_a, \rho c_p)$. The effects of laser absorption coefficient and temperature coefficient are completely ruled out in Θ. The laser power used in the experiment is very low to control the temperature rise of CFs at a moderate level. In this work, ρc_p and κ_a of the sample are measured by using the TET technique. Then, Θ is only related to the unknown κ_r of CF. Based on the different contribution of heat conduction under the two energy transport states, Θ could be used to determine κ_r. A 3D heat conduction model is used to simulate the temperature rise under the two energy transport states. A relationship between Θ and κ_r of CF could then be built to obtain the theoretical curve of Θ against κ_r. Then, the experimental Θ is interpolated into the curve to determine κ_r. And this FET-Raman technique has been verified by comparing the experimental results with that of other methods in our previous study. Based on our previous study, the modulation frequency should be selected to make Θ fall within the range of 0.7–0.8 to have a small measurement uncertainty [41].

In our FET-Raman measurement, for the steady-state heating, the energy transport in the sample is governed by the differential equation [42,43] as below:

$$\kappa_a \frac{\partial^2 T_{CW}}{\partial x^2} + \frac{1}{r}\cdot\frac{\partial}{\partial r}\cdot\left(r\cdot\kappa_r\cdot\frac{\partial T_{CW}}{\partial r}\right) + \dot{q} = 0, \tag{3}$$

where T_{CW} (K) is the temperature rise in steady-state heating, $\dot{q}$ volumetric Gaussian beam heating and is given as:

$$\dot{q}(r,z) = \frac{I_0}{\tau_L}\exp\left(-\frac{r_l^2}{r_0^2}\right)\exp\left(-\frac{z_l}{\tau_L}\right), \tag{4}$$

where $I_0 = P/\pi r_0^2$ is the laser power per unit area at the center of laser spot, r_0 (μm) the radius of the CW laser spot, r_l radial position from the center of the laser spot, τ_L the laser absorption depth and could be obtained based on the equation $\tau_L = \lambda/(4\pi k_L)$ [44], where λ (532 nm) is the laser wavelength, k_L the extinction coefficient of CF, and z_l the distance from the sample surface in the laser incidence direction. We have τ_L(CF) = 34.7 nm [45].

For the frequency-resolved state, the energy transport in CF is governed by the differential equation [46] as below:

$$\kappa_a \frac{\partial^2 T_{FR}}{\partial x^2} + \frac{1}{r}\cdot\frac{\partial}{\partial r}\cdot\left(r\cdot\kappa_r\cdot\frac{\partial T_{FR}}{\partial r}\right) + \dot{q} = \rho c_p \frac{\partial T_{FR}}{\partial t}, \tag{5}$$

where T_{FR} is the temperature rise in the transient state and $\dot{q}$ could be calculated using Eq. (4). By solving Eqs. (3) and (5), the ratio of temperature rise of CF under the two heating states could be obtained. In our experiments, this ratio is equal to the measured Θ. As κ_a and ρc_p are obtained from the TET experiments, Θ could be used to determine κ_r based on the different contribution of heat conduction under the two energy transport states. Based on Eq. (4), the Raman signal from various depths in the radial direction is considered. And for the frequency-resolved state, the Raman signal at different time is also considered. That is, the experimental Θ basically is based on Raman intensity-weighted temperature rise in both time and space. All these are also considered in our 3D heat conduction model as we do in the previous study [47].

4. Experimental details

In the TET experiment, a current source (Keithley 6221) is used to generate a small step current. And this current is applied to the sample shown in Fig. 3(a). The length and diameter of the sample are 1.82 mm and 53.9 μm, respectively. And an oscilloscope (Tektronix DPO3052) is used to measure the voltage variation during the Joule heating process. Fig. 3(b) shows the measured voltage variation of the sample.

In the Raman experiment, RT Raman spectra are collected automatically under different laser power to get the RSC. A 20 × objective lens is used for the two energy transport states, one lower and one higher laser power are used to irradiate CF. As shown

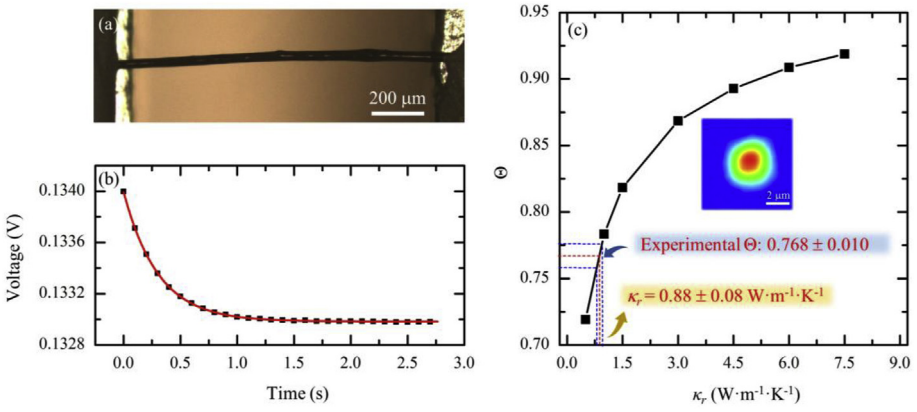

Fig. 3. **(a)** Microscopy image of one CF sample in TET measurement. **(b)** Measured voltage variation of the sample during the TET characterization and the fitting. The black symbols are the experiment data and the red line is the fitting curve. **(c)** The theoretical curve based on the ratio of temperature rise under two energy transport states against the different radial thermal conductivities of the sample used in the simulation. The inset shows the laser spot used in the experiment. The radial thermal conductivity of the CF is then determined by interpolating the experimental result into the curve. (A colour version of this figure can be viewed online.)

in Fig. 3(c), the diameter of the laser spot is also measured by using a high-resolution CCD camera of the microscope. The two laser powers should be maintained as low as possible to control the temperature rise at a moderate level and to stay within the linear temperature dependence range of the Raman shift. Raman experiments using the two laser powers are repeated 45 times, and the corresponding Θ values are obtained. Then these values are averaged to increase the accuracy of the experimental results.

A 3D numerical modeling based on the finite volume method is conducted to calculate the temperature rise under the two energy transport states to determine κ_r. The 3D numerical modeling process is similar to that reported in our previous work [48]. Similarly, a Raman intensity weighted average temperature rise over space under stead state and a Raman intensity weighted average temperature rise over space and time under frequency-resolved state are obtained. Then the ratio of these two values is used to determine the theoretical Θ against κ_r. The averaged Θ from the experiments could be interpolated to determine κ_r of CF.

5. Results and discussion

5.1. Representative sample for the anisotropic thermal characterization

Based on the measured voltage variation shown in Fig. 3(b), the normalized voltage variation, which is $V^*(t) = [V(t) - V_0]/[V(t\rightarrow\infty) - V_0]$, can be used to mimic the temperature variation. Here, V_0 is the initial voltage and $V(t\rightarrow\infty)$ is the steady state voltage. Then α_{eff} can be obtained to determine α_a and κ_a, which are measured at $1.10\times10^{-6}\,m^2\,s^{-1}$ and $2.15\,W\,m^{-1}\,K^{-1}$ for this selected CF. Based on the theoretical curve of Θ against κ_r and the experimental ratio shown in Fig. 3(c), κ_r of the selected CF is $0.88\,W\,m^{-1}\,K^{-1}$. Based on the results of TET experiment and Raman experiment, κ_r and κ_a are very much different. That is, the anisotropy of thermal conductivities in the radial and axial directions exists. And this anisotropy is highly related to the structure of the lignin-based CFs, which will be explained in detail in the following sections.

5.2. Variation of anisotropic thermal conductivities

To further verify the anisotropy of thermal conductivities in the two directions, four CFs (named S1, S2, S3, and S4) are used, and three positions (named P1, P2, and P3) are selected on each CF. All these results are summarized in Table 1. The uncertainty of these results is about 10%. Note that κ_a obtained from the TET technique is an average value of the CF. Among different CFs, the κ_a values are all around $1.4–2.15\,W\,m^{-1}\,K^{-1}$ at RT. Considering the structure difference among samples, the axial thermal conductivities show good consistency with each other. As a result, we can assume that the structure of the CF in the axial direction (termed "axial structure") is uniform. This structure assumption will be verified in section 5.4. Based on this assumption, the κ_a values at different positions of the same CF should be the same. The FET-Raman technique is used to measure κ_r at different positions of the same CF, and the κ_r of different CFs. Table 1 shows that the anisotropy of the thermal conductivities in the two directions exists for all the four CFs. As shown in Table 1, the κ_r values at different positions of the same CF are also very different, which indicates that the structure of CF in the radial direction (termed "radial structure") is not only different for different CFs, but also different at different axial positions of the same CF. For S1, the κ_r values at three different positions are all larger than κ_a, which means the degree of radial structure order is higher. For S2, the κ_r values at three positions are all much smaller than κ_a, which means the degree of radial structure order is much lower. However, for S3 and S4, the κ_r values at some positions are smaller than κ_a, while at some positions are larger than κ_a. All these results indicate that the radial structure order varies in a large range. As the lattice spacing of (002) peak for pristine graphite is about 0.335 nm [49], L_c of the CF is about 1.2 nm. This indicates that three layers or less exist in one crystallite unit. As L_c is larger than three times lattice spacing of pristine graphite, defective regions and cross-links may exist in the crystallite. And due to the different distribution of these defective regions and cross-links in different CFs, κ_r will also vary much. Though the lignin-based microscale CFs may vary from sample to sample, the value of this work is that we realize the axial and radial thermal conductivity measurement of CFs for the first time, and uncover the anisotropy for the same sample.

5.3. Effect of temperature on anisotropic thermal conductivities

Sample S2 is used to explore the effect of temperature on anisotropic thermal conductivities. For the TET experiments, the temperature ranges from 10.4 K to RT for this temperature effect study. The sample is suspended between two gold coated silicon electrodes and connected using small amount of silver paste. Then the sample is put in the vacuum chamber, where the air pressure is maintained below 0.5 mTorr. Fig. 4(a) shows the $V\sim t$ profiles at different temperatures. As shown in Fig. 4(a), the initial and steady state voltages are different at different temperatures. This is caused by two factors: the difference among the step currents applied to the sample at different temperatures, and the temperature induced change of the electrical resistance of the CF. Although the initial and steady state voltages are different, the characteristic time, which refers to the transient time in the $V\sim t$ curves, is not affected by the difference. Since the length (L) of the sample is much larger than the phonon mean free path (Λ), the thermal transport is taken as diffusive transport. Therefore, κ_a is determined by various scattering mechanism. That is, the phonons are scattered by other phonons, grain boundaries, and defects. Then the phonon relaxation time can be approximated as: $\tau^{-1} = \tau_U^{-1} + \tau_b^{-1} + \tau_d^{-1}$ [24], where τ_U, τ_b, and τ_d are phonon relaxation time due to phonon-phonon scattering (Umklapp scattering), phonon-boundary scattering, and phonon-defect scattering, respectively. Then, Λ can be related to τ as: $\Lambda = v\tau$, where v is the phonon group velocity. The axial thermal conductivity can be determined based on $\kappa_a = 1/3\rho c_p v\Lambda$. Therefore, the variation of κ_a against temperature contains information about specific heat as well as phonon scattering.

Due to the temperature dependence of heat capacity, the phonon scattering information cannot be obtained evidently from thermal conductivity. To get rid of the effect of heat capacity, the

Table 1
Summary of κ_r and κ_a of four CF samples.

Sample Index	S1			S2			S3			S4		
Position Index	P1	P2	P3	P1	P2	P3	P1	P2	P3	P1	P2	P3
κ_r($W\cdot m^{-1}\cdot K^{-1}$)	8.0	7.6	5.5	0.19	0.11	0.21	0.82	4.9	3.3	0.51	1.5	7.5
κ_a($W\cdot m^{-1}\cdot K^{-1}$)	1.4			1.6			1.85			2.15		

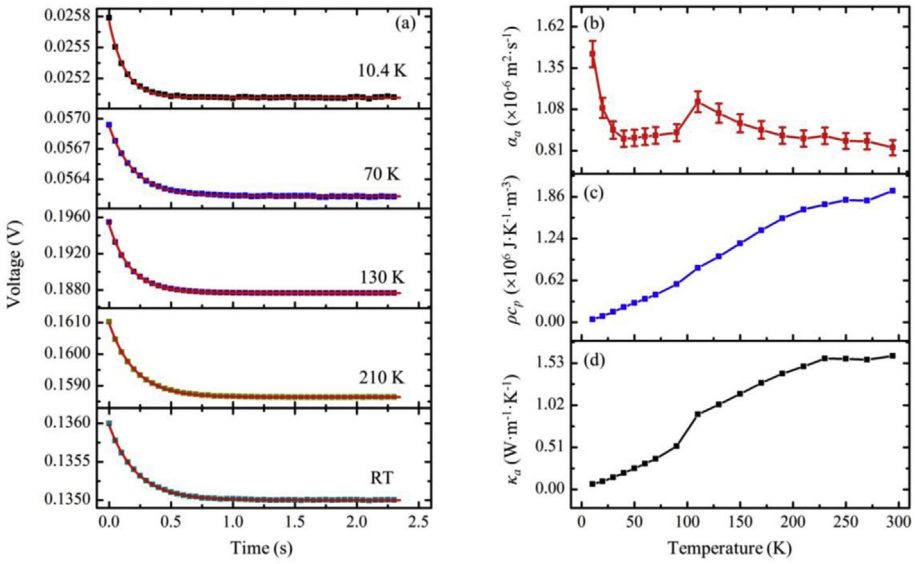

Fig. 4. **(a)** The TET voltage profiles for CF at different temperatures: RT (295 K), 210 K, 130 K, 70 K, and 10.4 K respectively. The symbols are the experiment data and the red lines are the fitting curves. **(b)** Temperature dependence of the axial thermal diffusivity for CF from RT to 10.4 K. Standard deviation of the thermal diffusivity is also shown in the figure. **(c)** Temperature dependence of the volumetric heat capacity for CF from RT to 10.4 K. **(d)** Temperature dependence of the axial thermal conductivity for CF from RT to 10.4 K. (A colour version of this figure can be viewed online.)

thermal diffusivity is more suitable for uncovering the phonon scattering mechanism. α_a can be expressed as $\alpha_a = (\nu\Lambda)/3 = (\nu^2\tau)/3$. Due to the three different phonon scattering processes, α_a can then be written as a function of phonon relaxation time as:

$$\alpha_a^{-1} = 3\Big/\nu^2 \cdot \left(\tau_U^{-1} + \tau_b^{-1} + \tau_d^{-1}\right) \tag{6}$$

ν changes little with temperature. τ_U is strongly dependent on temperature, while τ_b and τ_d are related to the structure of CF. The variation of α_a against temperature for the sample is shown in Fig. 4(b). Phonons are the main heat carriers in CF. Phonon-phonon scattering, phonon-defect scattering and phonon-boundary scattering are the three main mechanisms controlling the axial thermal diffusivity. At RT, with the high population of phonons, phonon-phonon scattering plays a major factor in the thermal transport. With the decrease of temperature, lattice vibration weakens and the phonon population decreases. Then, the phonon-phonon scattering intensity is reduced, and the phonon mean free path increases, which results in an increase of τ_U. As a result, α_a increases as temperature goes down from RT to around 130 K. With the further decrease of temperature, phonon-defect scattering and phonon-boundary scattering play a much more important role. The decrease of α_a is due to the low-temperature induced structural change in the CF. Based on the structure characterization of CF, the levels of defects at different positions are different, which indicates that the thermal expansion coefficients at these positions are different. Temperature reduction can induce thermal expansion mismatch, which results in the increase of phonon-defect scattering intensity. Thus, when temperature decreases further from 130 K to around 40 K, α_a starts to decrease. As temperature goes down to below 40 K, the phonon-phonon scattering intensity will decrease dramatically, the overall phonon scattering of the three mechanisms will also decrease. As a result, α_a increases quickly when the temperature decreases from 40 K to 10.4 K.

In the TET experiments, thermal diffusivity measurements of the CF under every temperature are repeated for 30 to 40 times. Then the standard deviation can be calculated out based on these results. And the relative errors of axial thermal diffusivity are also shown in Fig. 4(b). Based on the α_{eff} and κ_{eff} under different temperatures, the corresponding ρc_p values are obtained. Fig. 4(c) shows the variation of ρc_p against temperature. When the temperature decreases from RT to 10.4 K, ρc_p also decreases. Then the variation of κ_a against temperature is determined. As shown in Fig. 4(d), κ_a decreases from 1.6 to 0.06 W m^{-1} K^{-1} when the temperature decreases from RT to 10.4 K. The κ_a-T profile shows a monotonically decreasing behavior as temperature goes down. And κ_a tends to reach zero as the temperature decreases to 0 K. Due to the temperature dependence of ρc_p, the variations of α_a and κ_a against temperature are different. As a result, the two turning points in the α_a-T profile are not very visible in the κ_a-T profile.

For the FET-Raman experiments, the temperature ranges from 77 K to RT. The sample is put in an environmental cell, and liquid N_2 is used to cool the cell. As a result, the cell can be cooled as low as 77 K. By using this cell, the temperature can be adjusted precisely from 77 K to RT with a resolution of 1K. Fig. 5(a) shows the temperature dependence of radial thermal conductivity. As shown in this figure, κ_r values under different temperatures are all around 0.6 W m^{-1} K^{-1}. When temperature decreases from RT to 77 K, the radial thermal conductivity of the CF changes little throughout the entire temperature range although κ_a reduces by 75% when temperature changes from RT to 77 K.

As shown in Fig. 5(a), the laser spot size under each temperature is also measured and used in modeling to ensure highest accuracy of the experimental results. Fig. 5(b) is a 2D contour map of the Raman signal at different temperatures. As shown in this figure, Raman shift is redshifted with the increase of temperature. Raman spectra of CF at different temperatures are shown in Fig. 5(c). It can also be seen that both Raman peaks of CF are redshifted with the increase of temperature. The Raman spectra show two wide and overlapped peaks at 1350 and 1580 cm^{-1}, corresponding to D peak and G peak for the sample. And the ratio of these two peak intensities I_D/I_G can be used to reflect the degree of defects in the CF. With the increase of this ratio, the degree of defects also increases.

As the variation of κ_r against temperature carries information about specific heat and phonon scattering, the radial thermal diffusivity (α_r) is also used to study the temperature effect. The

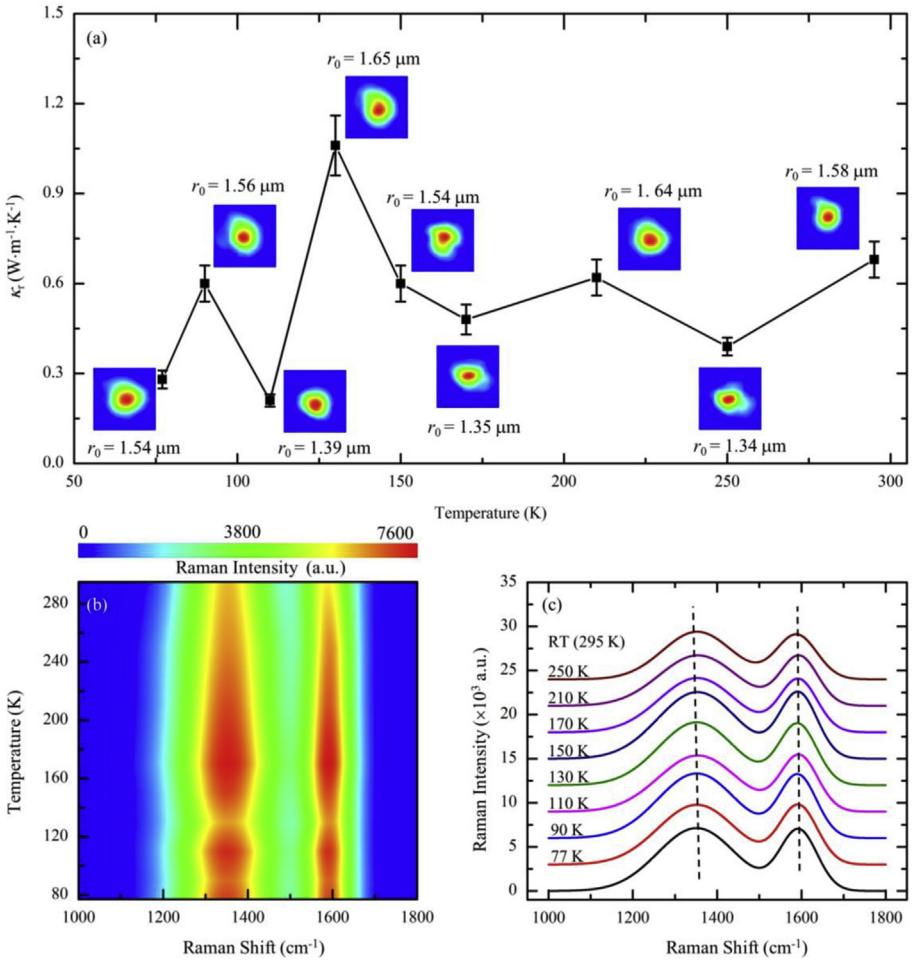

Fig. 5. **(a)** Temperature dependence of the radial thermal conductivity for CF from RT to 77 K. The laser spots at different temperatures are also shown in this figure. **(b)** 2D contour map to demonstrate the variation of Raman shift against temperature. **(c)** Raman spectra of CF at different temperatures. (A colour version of this figure can be viewed online.)

variation of α_r against temperature for the sample is shown in Fig. 6(a). Like α_a, α_r is also related to phonon-phonon scattering, phonon-defect scattering, and phonon-boundary scattering. When the temperature decreases from RT to 130 K, α_r increases from 0.35×10^{-6} to 1.09×10^{-6} m^2, which is also due to the reduced phonon-phonon scattering intensity. With the further decrease of temperature, phonon-defect scattering is the major factor. The variation of I_D/I_G against temperature, which can be used to reflect the degree variation of defects, is shown in Fig. 6(b). As shown in this figure, the degree of defects has a small change with the decrease of temperature. However, when temperature decreases to 130 K or lower, the variation of α_r is dominated by the phonon-defect scattering. Even a small structure change can also affect the variation of α_r.

Fig. 6(a) and (b) show that when the degree of defects increases, the phonon-defect scattering intensity increases, and α_r decreases. Considering the temperature dependence of volumetric heat capacity, we can conclude that the radial thermal conductivity shows very week temperature dependence based on the relation $\kappa_r = \rho c_p \alpha_r$.

5.4. Anisotropic structure of the carbon fiber uncovered by Raman spectrum

We speculate that the anisotropy of the thermal conductivities in the two directions are due to the structure difference between these two directions. This has been verified by Raman spectrum in multi-layered graphene, graphene paper, and highly-ordered pyrolytic graphite (HOPG) [50]. Compared with that from the top view, the Raman spectrum from the side of sample shows a weaker 2D peak for graphene, split in the G peak and invisible split in the 2D peak for HOPG. Here we use graphene paper to first prove that the Raman spectra are indeed different when the structure is anisotropic and the Raman spectra are taken from different orientations of the sample. The graphene paper used here is highly anisotropic and consists of extremely ordered graphene flakes of 5–6 layers [51,52]. As shown in Fig. 7, Raman spectra of different positions from top view and side view are obtained for graphene paper. G and D + D″ peaks exist in both two spectra. Tiny D and D + D′ peaks, two extra peaks at 1450 cm^{-1} and 1517 cm^{-1} are detected in the Raman spectra from side view. The D and G peaks correspond to transverse optical (TO) phonons near the K point and to optical E_{2g} phonons at the Brillouin zone center, respectively. Both the D and G peaks arise from vibrations of sp^2-hybridized carbon atoms [53]. And the D + D″ peak, which lies at around 2430 cm^{-1}, is the double Raman resonance of both the aforementioned TO phonons and the longitudinal acoustic (LA) phonons along the Γ-K direction [54]. Fig. 7 shows that D + D′ peak has a much higher intensity in the Raman spectrum for the side than that from top view.

Based on the above verification, Raman spectra of sample S3 in the two directions are also collected and compared, shown in

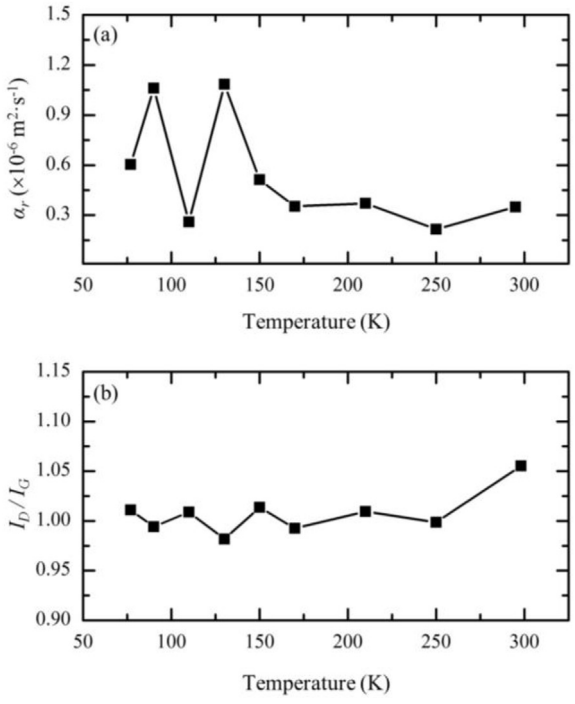

Fig. 6. **(a)** Radial thermal diffusivity of CF against temperature. **(b)** The variation of I_D/I_G against temperature.

Fig. 8(a) to study the structure anisotropy. For the cross-section measurement, the CF is not sliced by a saw. We just break the CF directly and collect the Raman spectra from the cross-section. Based on our previous study on silicon [55], the grain size at the edge or cross-section may be different from that at the side surface. Due to this difference, the corresponding Raman intensity can be different, while the types of Raman peaks cannot be altered. As shown in Fig. 8(a), the kinds of Raman peaks in the two directions are not the same, which indicates that the structure orientations are different in the two directions. As shown in Fig. 8(a), the D, G, D + D″ peaks, and the peak around 472 cm^{-1} exist in both two spectra. The peak observed at around 472 cm^{-1} is designated as the overtone of the L_1 mode. The L_1 mode is strongly dependent on the excitation energy and has the same polarization behavior as the G mode. And this laser-energy-dependent mode is the resonantly enhanced phonons in the TA phonon branches [29]. Fig. 8(a) shows that there are some differences for these peaks in both spectra. First, both D peak and G peak are sharper when the laser irradiates the side of the CF. Second, the Raman intensity of D peak is larger than that of G peak when the laser irradiates the side of the CF. While the Raman intensity of D peak is smaller than that of G peak when the laser irradiates the cross-section of the CF. Third, it is obvious that the D + D″ peak and the peak around 472 cm^{-1} detected from cross-section have a substantially higher intensity. This clearly demonstrates the difference between axial and radial structure orientations of CF. Similar Raman spectra difference is also found for graphene paper as discussed above, which has very strong anisotropic structure.

In addition to these differences among the peaks that co-exists in the two spectra, there are some Raman peaks only exist in the spectrum obtained from the cross-section of the CF. Two extra Raman peaks at 1450 cm^{-1} and 1517 cm^{-1} are detected for the cross-section Raman spectrum. In addition to the fundamental vibrations of alkyl functional groups, these two peaks represent mainly aromatic semi-quadrant ring breathing for aromatic ring systems having more than two fused benzene rings. The aromatic ring systems are typically found in amorphous carbon materials [56–58]. That is, these two peaks can be used to reflect the structure order of the detecting area. A tiny 2D peak at 2675 cm^{-1}, which

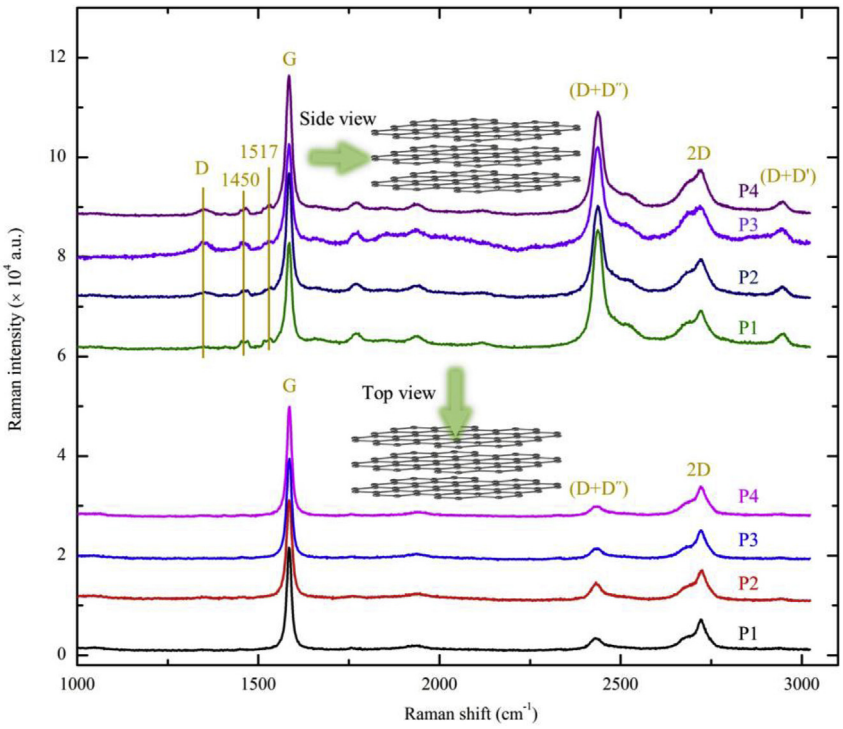

Fig. 7. Raman spectra of graphene paper at different positions from top view and side view. The top view and side view directions of the graphene paper are also shown in the figure, the green arrows show the laser incident directions. (A colour version of this figure can be viewed online.)

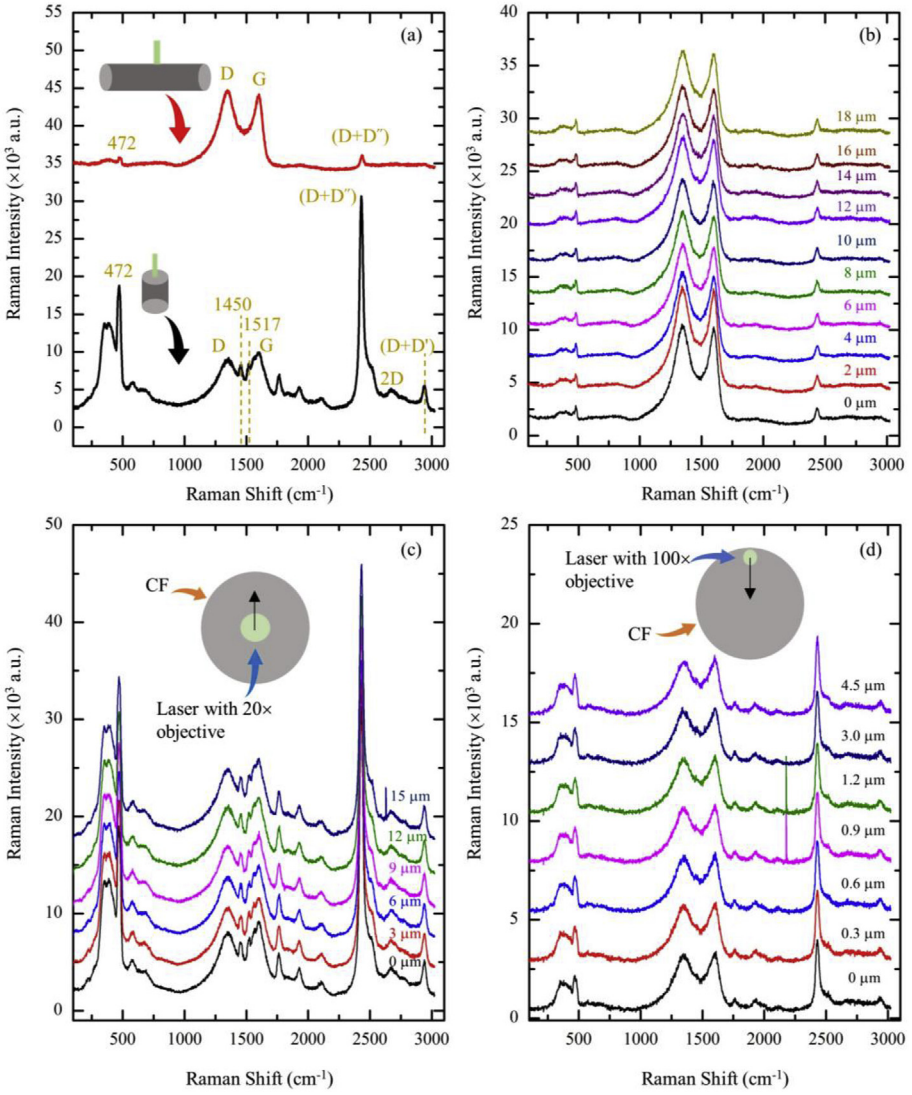

Fig. 8. **(a)** Raman spectra of CF measured from side and cross-section. **(b)** Raman spectra at different positions when the sample is scanned in the axial direction with a step of 2 μm. **(c)** Raman spectra at different positions when the sample is scanned in the radial direction with a step of 3 μm. And a 20 × objective lens is used for this scanning process. **(d)** Raman spectra at different positions when the sample is scanned in the radial direction with a step of 0.3 μm. And a 100 × objective lens is used for this scanning process. The starting positions of the Raman scanning and the objective lens used for these two scanning processes are also shown in these two figures. (A colour version of this figure can be viewed online.)

is an overtone of D peak, is also detected in the cross-plane direction. The shape of this peak can be used to identify monolayer graphene. As this peak is the sum of two phonons with opposite momentum, it is also present in the absence of any defects. In Fig. 8(a), there is also a peak at around 2940 cm^{-1}, called D + D′, which is a combination of two phonons with different momentum. The D′ peak occurs via an intravalley double-resonance process in the presence of defects [53]. All these differences reflect the structure orientation difference in the two directions, which leads to the anisotropic thermal conductivities in the two directions. To this point, we can firmly conclude that the carbon fiber has very anisotropic structure like that of graphene paper: the cross-section structure order is more like that of graphene when viewed from the side, and the axial direction structure order is more like the in-plane structure of graphene paper. Conclusively, the cross-plane thermal conductivity ($\kappa_\perp$) should be smaller than the in-plane thermal conductivity ($\kappa_\parallel$) for graphene paper. Based on our previous study, $\kappa_\parallel$ and $\kappa_\perp$ at RT are around 634 and 6 $W\,m^{-1}\,K^{-1}$, respectively [51,52]. Thus, the anisotropy of thermal conductivities in the two directions is also highly related to the difference of Raman spectra in the two directions.

In our experiment, we also speculate that the axial structure of CF is uniform. The Raman scanning technique developed by our group is used to scan the sample side along the axial direction and collect the Raman signal at each scanning position. The scanning step is 2 μm, and a total length of 18 μm is scanned. The collected ten Raman spectra at these ten positions are shown in Fig. 8(b). It can be seen that all these spectra are very similar, which indicates that the axial structures at different positions are close to each other.

The Raman scanning technique is also used to scan the sample in the cross-section, which is to show that the radial structure is quite uniform along the radial direction at one axial location. Fig. 8(c) shows the rough scanning results with a scanning step of 3 μm. The scanning direction is from the center of the cross-section to the side. As shown in this figure, there is almost no difference

among the spectra at different positions. However, this is not sufficient to conclude that the radial structure is also uniform.

To verify this, a fine scanning with an objective lens of 100 × magnification is also done in this direction. The scanning step is 0.3 μm, and the scanning direction is from the side to the center of the cross-section. As shown in Fig. 8(d), the Raman spectra collected at the positions close the side are the same with that at the internal positions. As a result, the radial structure in the cross-section at one axial location is firmly proved uniform. Conclusively, the CF has anisotropic structures in these two directions.

As shown in Table 1, there is a small difference among the κ_a values for the four CFs. To explain this difference, we study the Raman spectra at different axial locations of the four CFs measured from side. As shown in Fig. 9(a), the Raman intensities of D + D″ and D + D′ peaks decrease with the increase of κ_a. Based on the Raman spectra of graphene paper shown in Fig. 7, the Raman intensities of these two peaks are higher when the exciting laser irradiates the cross-plane direction.

As a result, the decrease of the Raman intensities of these two peaks from sample 1 to sample 4 indicates that the concentration of carbon nanocrystallites whose c-axis along the axial direction of the fiber is decreasing. That is, the axial structure order is increasing with the decrease of the Raman intensities of these two peaks. Consequently, κ_a increases with the decrease of the Raman intensities of these two peaks. Fig. 9(a) also shows that the Raman spectra at different positions of the same CF are nearly the same, which verifies the uniformity of the axial structure.

Based on the FET-Raman results, the κ_r values are different at different positions of one CF. To interpret this observation, we study the Raman spectra of cross-section at different axial locations. Fig. 9(b) shows the cross-section Raman spectra at four different cross-sections of sample S3. As shown in this figure, the Raman intensities of D + D″ peak, and peaks at 1450 cm^{-1} and 1517 cm^{-1} are different for the four positions, which indicates that the structure orders are different. It can be seen that the Raman intensities of 1450 cm^{-1} and 1517 cm^{-1} peaks at cross-section 2 are lower than those at the other three cross-sectional positions. And the Raman intensities of D + D″ peak at cross-section 2 and 3 are lower than

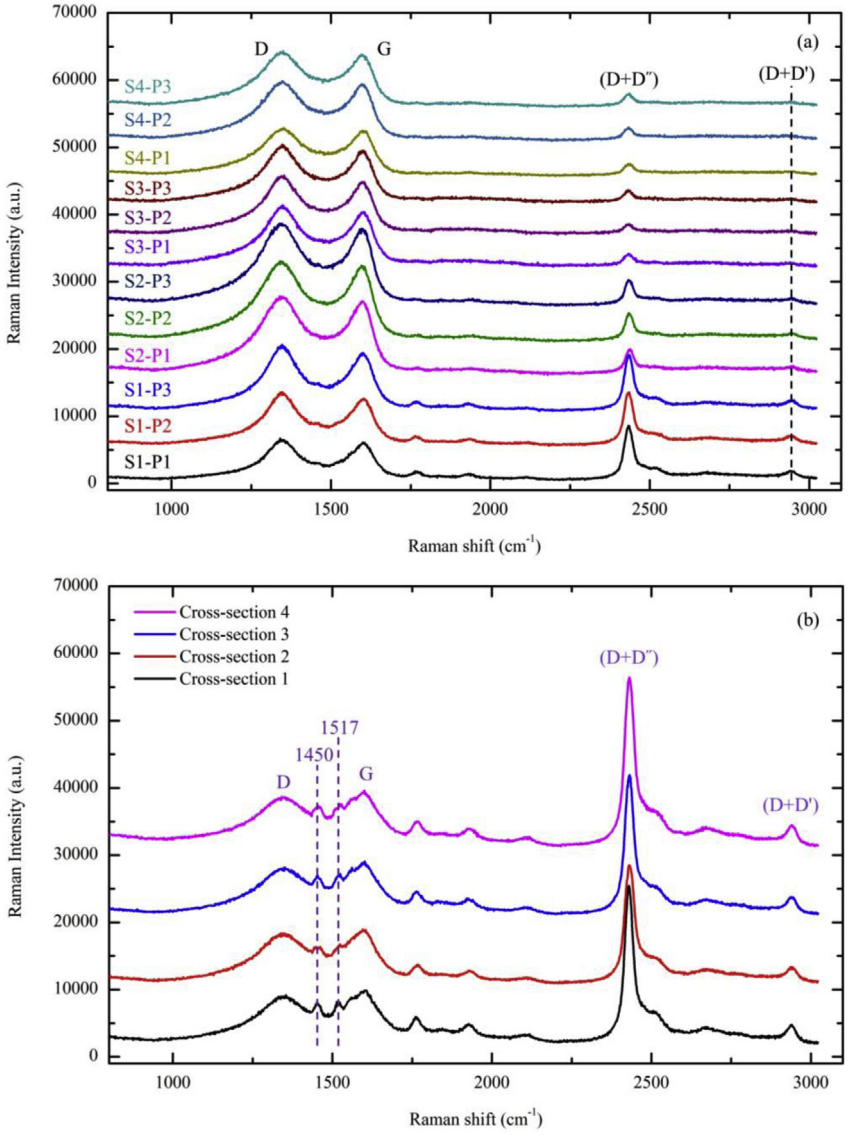

Fig. 9. **(a)** Raman spectra at different axial locations of the four CFs measured from side. **(b)** Raman spectra of sample S3 measured at cross-sections of different axial locations. (A colour version of this figure can be viewed online.)

those at the other two positions. While the Raman intensities of the D peak and G peak at the four positions are nearly the same. As a result, the structure order at cross-section 2 and 3 are lower than the other two positions. As the Raman intensities of the D peak and G peak at the four positions are nearly the same, the I_D/I_G values at the four positions are also nearly the same, that is, the degree of defects are nearly the same. In short, the difference of κ_r at different cross-sections is mainly induced by the different radial structure order at these positions.

Combining all these Raman scanning results, the structural components of the CF are believed to consist of carbon nanocrystallites, amorphous carbon, and nanopores [59]. The carbon nanocrystallites are regions of graphene layers, and the lattice vibration directions are different for these regions [60]. The amorphous carbon can be a mixture of carbon atoms trapped in the carbon nanocrystallites. The nanopores spread within the carbon nanocrystallites and amorphous carbon mixture.

6. Conclusion

In this work, a novel method by combining the FET-Raman technique and TET technique was developed to measure κ_a and κ_r of lignin-based CFs. Four carbon fibers were characterized using this method. Significant thermal conductivity anisotropy was observed. The κ_a values for all the four CFs were around 1.8 $W\,m^{-1}\,K^{-1}$, and the axial structure difference of these CFs was very small. The κ_r values could be as small as 0.11 $W\,m^{-1}\,K^{-1}$, or as large as 8.0 $W\,m^{-1}\,K^{-1}$, indicating that the radial structure difference of these fibers was very large. Even for the same carbon fiber, there was also a large difference in the κ_r values at different axial positions. With the decrease of temperature from RT to 10.4 K, κ_a decreased by more than order of magnitude. While the values of κ_r from RT down to 77 K showed very weak variation against temperature. All these were attributed to the anisotropic structures of this kind of carbon fiber. This anisotropy was verified by using a Raman scanning technique. The Raman spectra of the CF side and cross section showed significant difference, firmly confirming the structure anisotropy. The Raman scanning study uncovered that the axial structure was uniform along the axial direction and the radial structure was uniform along the radial direction. However, the radial structure showed differences at different axial locations. All these successfully explained the observed anisotropic thermal conductivities and the change of κ_r along the axial position.

Acknowledgement

Support of this work by the College of Engineering of Iowa State University is gratefully acknowledged.

References

[1] Z. Xu, C. Gao, Graphene fiber: a new trend in carbon fibers, Mater. Today 18 (9) (2015) 480–492.
[2] E. Frank, L.M. Steudle, D. Ingildeev, J.M. Sporl, M.R. Buchmeiser, Carbon fibers: precursor systems, processing, structure, and properties, Angew Chem. Int. Ed. Engl. 53 (21) (2014) 5262–5298.
[3] R. Jeffries, Prospects for carbon fibres, Nature 232 (1971) 304–307.
[4] Jean-Baptiste Donnet, T.K.W, Serge Rebouillat, Jimmy C.M. Peng, Carbon Fibers, third ed. ed., CRC Press, 1998.
[5] E. Fitzer, Pan-based carbon fibers – present state and trend of the technology from the viewpoint of possibilities and limits to influence and to control the fiber properties by the process parameters, Carbon 27 (5) (1989) 621–645.
[6] A.A. Bright, L.S. Singer, The electronic and structural characteristics of carbon fibers from mesophase pitch, Carbon 17 (1) (1979) 59–69.
[7] M. Endo, Structure of mesophase pitch-based carbon fibres, J. Mater. Sci. 23 (2) (1988) 598–605.
[8] F. Souto, V. Calado, N. Pereira, Lignin-based carbon fiber: a current overview, Mater. Res. Express 5 (7) (2018) 072001.
[9] H. Mainka, O. Täger, E. Körner, L. Hilfert, S. Busse, F.T. Edelmann, A.S. Herrmann, Lignin – an alternative precursor for sustainable and cost-effective automotive carbon fiber, Journal of Materials Research and Technology 4 (3) (2015) 283–296.
[10] J.F. Kadla, S. Kubo, R.A. Venditti, R.D. Gilbert, A.L. Compere, W. Griffith, Lignin-based carbon fibers for composite fiber applications, Carbon 40 (15) (2002) 2913–2920.
[11] F.S. Igor Maria De Rosa, Maria Sabrina Sarto, Alessio Tamburrano, EMC impact of advanced carbon fiber/carbon nanotube reinforced composites for next-generation aerospace applications, IEEE Transactions on Electronmagnetic Compatibility 50 (3) (2008) 556–563.
[12] R. Naslain, Design, preparation and properties of non-oxide CMCs for application in engines and nuclear reactors: an overview, Compos. Sci. Technol. 64 (2) (2004) 155–170.
[13] J. Paquette, J. van Dam, S. Hughes, Structural testing of 9m carbon fiber wind turbine research blades, in: 45th AIAA Aerospace Sciences Meeting and Exhibit, Reno, Nevada, 2007, p. 11.
[14] T. Windhorst, G. Blount, Carbon-carbon composites: a summary of recent developments and applications, Mater. Des. 18 (1) (1997) 11–15.
[15] Z.L. Wang, D.W. Tang, W.G. Zhang, Simultaneous measurements of the thermal conductivity, thermal capacity and thermal diffusivity of an individual carbon fibre, J. Phys. Appl. Phys. 40 (15) (2007) 4686–4690.
[16] X. Zhao, X. Lu, W.T.Y. Tze, P. Wang, A single carbon fiber microelectrode with branching carbon nanotubes for bioelectrochemical processes, Biosens. Bioelectron. 25 (10) (2010) 2343–2350.
[17] X. Zhang, S. Fujiwara, M. Fujii, Measurements of thermal conductivity and electrical conductivity of a single carbon fiber, Int. J. Thermophys. 21 (4) (2000) 965–980.
[18] N.C. Gallego, D.D. Edie, B. Nysten, J.P. Issi, J.W. Treleaven, G.V. Deshpande, The thermal conductivity of ribbon-shaped carbon fibers, Carbon 38 (7) (2000) 1003–1010.
[19] J. Wang, M. Gu, W. Ma, X. Zhang, Y. Song, Temperature dependence of the thermal conductivity of individual pitch-derived carbon fibers, N. Carbon Mater. 23 (3) (2008) 259–263.
[20] F.G. Emmerich, Young's modulus, thermal conductivity, electrical resistivity and coefficient of thermal expansion of mesophase pitch-based carbon fibers, Carbon 79 (2014) 274–293.
[21] C. Pradere, J.C. Batsale, J.M. Goyhénèche, R. Pailler, S. Dilhaire, Thermal properties of carbon fibers at very high temperature, Carbon 47 (3) (2009) 737–743.
[22] L. Qiu, X.H. Zheng, J. Zhu, G.P. Su, D.W. Tang, The effect of grain size on the lattice thermal conductivity of an individual polyacrylonitrile-based carbon fiber, Carbon 51 (2013) 265–273.
[23] G. Yuan, X. Li, Z. Dong, A. Westwood, B. Rand, Z. Cui, Y. Cong, J. Zhang, Y. Li, Z. Zhang, J. Wang, The structure and properties of ribbon-shaped carbon fibers with high orientation, Carbon 68 (2014) 426–439.
[24] J. Liu, W. Qu, Y. Xie, B. Zhu, T. Wang, X. Bai, X. Wang, Thermal conductivity and annealing effect on structure of lignin-based microscale carbon fibers, Carbon 121 (2017) 35–47.
[25] A.S. Pollard, M.R. Rover, R.C. Brown, Characterization of bio-oil recovered as stage fractions with unique chemical and physical properties, J. Anal. Appl. Pyrol. 93 (2012) 129–138.
[26] W. Qu, Y. Xue, Y. Gao, M. Rover, X. Bai, Repolymerization of pyrolytic lignin for producing carbon fiber with improved properties, Biomass Bioenergy 95 (2016) 19–26.
[27] H.C. Schniepp, J.-L. Li, M.J. McAllister, H. Sai, M. Herrera-Alonso, D.H. Adamson, R.K. Prud'homme, R. Car, D.A. Saville, I.A. Aksay, Functionalized single graphene sheets derived from splitting graphite oxide, J. Phys. Chem. B 110 (17) (2006) 8535–8539.
[28] J. Heremans, I. Rahim, M.S. Dresselhaus, Thermal conductivity and Raman spectra of carbon fibers, Phys. Rev. B 32 (10) (1985) 6742–6747.
[29] P. Tan, C. Hu, J. Dong, W. Shen, B. Zhang, Polarization properties, high-order Raman spectra, and frequency asymmetry between Stokes and anti-Stokes scattering of Raman modes in a graphite whisker, Phys. Rev. B 64 (21) (2001) 214301.
[30] E. Franklin Rosalind, T. Randall John, Crystallite growth in graphitizing and non-graphitizing carbons, Proc. Roy. Soc. Lond. Math. Phys. Sci. 209 (1097) (1951) 196–218.
[31] I.Y. Stein, Synthesis and Characterization of Next-Generation Multifunctional Material Architectures: Aligned Carbon Nanotube Carbon Matrix Nanocomposites, Massachusetts Institute of Technology, Cambridge, 2013.
[32] B. Nysten, J.P. Issi, R. Barton, D.R. Boyington, J.G. Lavin, Determination of lattice defects in carbon fibers by means of thermal-conductivity measurements, Phys. Rev. B 44 (5) (1991) 2142–2148.
[33] J. Guo, X. Wang, T. Wang, Thermal characterization of microscale conductive and nonconductive wires using transient electrothermal technique, J. Appl. Phys. 101 (6) (2007) 063537.
[34] J. Guo, X. Wang, L. Zhang, T. Wang, Transient thermal characterization of micro/submicroscale polyacrylonitrile wires, Appl. Phys. A 89 (1) (2007) 153–156.
[35] B. Zhu, J. Liu, T. Wang, M. Han, S. Valloppilly, S. Xu, X. Wang, Novel polyethylene fibers of very high thermal conductivity enabled by amorphous restructuring, ACS Omega 2 (7) (2017) 3931–3944.
[36] B. Zhu, R. Wang, S. Harrison, K. Williams, R. Goduguchinta, J. Schneiter, J. Pegna, E. Vaaler, X. Wang, Thermal conductivity of SiC microwires: effect of temperature and structural domain size uncovered by 0 K limit phonon

scattering, Ceram. Int. 44 (10) (2018) 11218–11224.
[37] Y. Sekii, T. Hayashi, Measurements of reflectance and thermal emissivity of a black surface created by electrostatic flocking with carbon-fiber piles, IEEE Trans. Dielectr. Electr. Insul. 16 (3) (2009) 649–654.
[38] Y. Xie, T. Wang, B. Zhu, C. Yan, P. Zhang, X. Wang, G. Eres, 19-Fold thermal conductivity increase of carbon nanotube bundles toward high-end thermal design applications, Carbon 139 (2018) 445–458.
[39] T. Wang, S. Xu, D.H. Hurley, Y. Yue, X. Wang, Frequency-resolved Raman for transient thermal probing and thermal diffusivity measurement, Opt. Lett. 41 (1) (2016) 80–83.
[40] T. Wang, M. Han, R. Wang, P. Yuan, S. Xu, X. Wang, Characterization of anisotropic thermal conductivity of suspended nm-thick black phosphorus with frequency-resolved Raman spectroscopy, J. Appl. Phys. 123 (14) (2018) 145104.
[41] H. Zobeiri, R. Wang, T. Wang, H. Lin, C. Deng, X. Wang, Frequency-domain energy transport state-resolved Raman for measuring the thermal conductivity of suspended nm-thick MoSe2, Int. J. Heat Mass Transf. 133 (2019) 1074–1085.
[42] P. Yuan, J. Liu, R. Wang, X. Wang, The hot carrier diffusion coefficient of sub-10 nm virgin MoS_2: uncovered by non-contact optical probing, Nanoscale 9 (20) (2017) 6808–6820.
[43] J.-U. Lee, D. Yoon, H. Kim, S.W. Lee, H. Cheong, Thermal conductivity of suspended pristine graphene measured by Raman, Phys. Rev. B 83 (8) (2011) 081419.
[44] X. Chen, X. Wang, Microscale spatially resolved thermal response of Si nanotip to laser irradiation, J. Phys. Chem. C 115 (45) (2011) 22207–22216.
[45] J.W. Weber, V.E. Calado, M.C.M. van de Sanden, Optical constants of graphene measured by spectroscopic ellipsometry, Appl. Phys. Lett. 97 (9) (2010) 091904..
[46] S. Sinha, Thermal model for nanosecond laser ablation of alumina, Ceram. Int. 41 (5) (2015) 6596–6603.
[47] R. Wang, T. Wang, H. Zobeiri, P. Yuan, C. Deng, Y. Yue, S. Xu, X. Wang, Measurement of thermal conductivity of suspended MoS_2 and $MoSe_2$ by nanosecond ET-Raman free of temperature calibration and laser absorption evaluation, Nanoscale 10 (2018) 23087–23102.
[48] R. Wang, T. Wang, H. Zobeiri, P. Yuan, C. Deng, Y. Yue, S. Xu, X. Wang, Measurement of the thermal conductivities of suspended MoS_2 and $MoSe_2$ by nanosecond ET-Raman without temperature calibration and laser absorption evaluation, Nanoscale 10 (2018) 23087–23102.
[49] H.R. Palser, A, Interlayer interactions in graphite and carbon nanotubes, Phys. Chem. Chem. Phys. 1 (18) (1999) 4459–4464.
[50] Z. Li, R.J. Young, I.A. Kinloch, N.R. Wilson, A.J. Marsden, A.P.A. Raju, Quantitative determination of the spatial orientation of graphene by polarized Raman spectroscopy, Carbon 88 (2015) 215–224.
[51] M. Han, Y. Xie, J. Liu, J. Zhang, X. Wang, Significantly reduced c-axis thermal diffusivity of graphene-based papers, Nanotechnology 29 (26) (2018) 265702.
[52] Y. Xie, P. Yuan, T. Wang, N. Hashemi, X. Wang, Switch on the high thermal conductivity of graphene paper, Nanoscale 8 (40) (2016) 17581–17597.
[53] D.C. Elias, R.R. Nair, T.M.G. Mohiuddin, S.V. Morozov, P. Blake, M.P. Halsall, A.C. Ferrari, D.W. Boukhvalov, M.I. Katsnelson, A.K. Geim, K.S. Novoselov, Control of graphene's properties by reversible hydrogenation: evidence for graphane, Science 323 (5914) (2009) 610–613.
[54] S. Sullivan, A. Vallabhaneni, I. Kholmanov, X. Ruan, J. Murthy, L. Shi, Optical generation and detection of local nonequilibrium phonons in suspended graphene, Nano Lett. 17 (3) (2017) 2049–2056.
[55] S. Xu, X. Tang, Y. Yue, X. Wang, Sub-micron imaging of sub-surface nanocrystalline structure in silicon, J. Raman Spectrosc. 44 (11) (2013) 1523–1528.
[56] D.M. Keown, X. Li, J.-i. Hayashi, C.-Z. Li, Characterization of the structural features of char from the pyrolysis of cane trash using fourier transform–Raman spectroscopy, Energy Fuels 21 (3) (2007) 1816–1821.
[57] X. Li, J. Hayashi, C. Li, FT-Raman spectroscopic study of the evolution of char structure during the pyrolysis of a Victorian brown coal, Fuel 85 (12–13) (2006) 1700–1707.
[58] J. Schwan, S. Ulrich, V. Batori, H. Ehrhardt, S.R.P. Silva, Raman spectroscopy on amorphous carbon films, J. Appl. Phys. 80 (1) (1996) 440–447.
[59] X. Zhang, Q. Yan, W. Leng, J. Li, J. Zhang, Z. Cai, E.B. Hassan, Carbon manostructure of Kraft lignin thermally treated at 500 to 1000 degrees C, Materials 10 (8) (2017) 975.
[60] J.S. McDonald-Wharry, M. Manley-Harris, K.L. Pickering, Reviewing, combining, and updating the models for the nanostructure of non-graphitizing carbons produced from oxygen-containing precursors, Energy Fuels 30 (10) (2016) 7811–7826.